RESEARCH ARTICLE | DECEMBER 11 2024

Flux-mediated effective Su–Schrieffer–Heeger model in an impurity decorated diamond chain

Special Collection: Angular Momentum of Light

D. Viedma ; A. M. Marques ; R. G. Dias ; V. Ahufinger

APL Photonics 9, 120801 (2024)
https://doi.org/10.1063/5.0232163

Flux-mediated effective Su–Schrieffer–Heeger model in an impurity decorated diamond chain

Cite as: APL Photon. 9, 120801 (2024); doi: 10.1063/5.0232163
Submitted: 5 August 2024 • Accepted: 25 November 2024 •
Published Online: 11 December 2024

D. Viedma,[1,a)] A. M. Marques,[2] R. G. Dias,[2] and V. Ahufinger[1]

AFFILIATIONS

[1] Departament de Física, Universitat Autònoma de Barcelona, E-08193 Bellaterra, Spain
[2] Department of Physics and i3N, University of Aveiro, 3810-193 Aveiro, Portugal

Note: This paper is part of the Special Topic on Angular Momentum of Light.
[a)] **Author to whom correspondence should be addressed:** david.viedma@uab.cat

ABSTRACT

In photonic flat-band (FB) systems, which are characterized by a halting of light transmission, perturbations can play a major role in determining the transport properties of the system. In this work, this is exploited by purposefully including impurities in a photonic diamond chain with a constant synthetic flux per plaquette so that an effective system of choice can be tailored from the FB. By tuning both the separation between impurities and the flux value, any coupling distribution can be engineered. The effective system can also exhibit a nontrivial topology as we demonstrate by imprinting a Su–Schrieffer–Heeger model on the diamond chain, which is further shown to have enhanced robustness to disorder due to the extension of the impurity modes. Furthermore, effective non-Hermitian systems can also be realized by employing complex-valued impurities. We propose an implementation of the system in a lattice of optical waveguides carrying orbital angular momentum modes, where a phase in the coupling can be included and controlled geometrically. There, variations of the refractive index of chosen waveguides generate detunings that act as impurities, which couple together to form the effective system. This work opens the way for the design of topologically nontrivial models in other FB systems, or in other physical platforms.

I. INTRODUCTION

Photonic flat-band (FB) systems[1,2] have garnered considerable attention in recent years as platforms to study and visualize fundamental light transport and localization properties, whose counterparts in condensed-matter analogs are considerably more challenging to observe.[3] Photonic FBs also have the potential for applications in varied topics such as dispersionless imaging,[4,5] slow light,[6–8] and enhancement of nonlinear processes.[9] Systems of coupled optical waveguides,[10,11] photonic crystals,[12,13] exciton-polaritons[14] and optically induced lattices in photorefractives,[15,16] among other diverse physical platforms,[17–21] have all been proven to be promising for the implementation of FB systems. FBs are, in general, characterized by an absence of transport, by virtue of them being completely dispersionless, and can arise due to the protection provided by a particular symmetry of the system or the fine-tuning of the parameters of the considered lattice.[22] The study of light localization in FBs is usually tied to the existence of compact localized states (CLS),[23] which are eigenmodes of the lattice with strictly zero field amplitudes beyond a finite number of unit cells. This localization occurs due to destructive interference over different coupling paths. Since FBs lack any transport of their own, a perturbation affecting them can have strong effects on the transport properties of the lattice.[22]

Our aim is to use this high sensitivity to perturbations to our advantage, with the final objective of imprinting a desired effective system by tailoring the FB. This is achieved by purposefully including impurities in the system: by adequately engineering the distribution of impurities, the properties of the effective system can be tuned, allowing to build a wide range of different models. Of particular interest is the ability to bestow these effective systems with a nontrivial topology, thus gaining access to topologically protected modes. In this work, we consider a photonic diamond chain lattice with a finite flux per plaquette, which possesses a gapped FB in the spectrum of propagation constants whose modes can be written as CLSs. By introducing diagonal impurities in a plaquette of the

chain, we perturb the CLSs with finite amplitude at that position. For nonzero flux, adjacent CLSs become coupled and generate a set of exponentially decaying impurity modes whose localization length depends on the flux.[24] Further decorating the lattice with additional impurities enables couplings between the corresponding impurity modes, whose strength can be controlled by the value of the flux and the distance between impurities. To showcase the method, we imprint a Su–Schrieffer–Heeger (SSH) model[25] by staggering the distances between impurities. We first briefly describe the theoretical method behind the formation of the effective system, which was introduced in Ref. 24 for a single impurity. Here, we instead focus on the generation of an effective system that is formed through the coupling of separate impurity modes. We place the spotlight on the appearance of the edge mode of the SSH model, which is localized around the end of the chain of impurities. We study its robustness against different types of disorder and show how it displays enhanced protection even against disorder that breaks its chiral symmetry due to the extension of the impurity modes.

Finally, we provide a possible route to implement the described system. We require a way to imprint a finite flux per plaquette onto a diamond chain, as well as a way to decorate this chain with controlled onsite impurities at certain sites. In photonics alone, several platforms have been shown to provide a controllable way to introduce these fluxes, such as ring resonators with different optical paths,[26–31] twisted or modulated lattices,[32–39] fiber loops,[40–42] and optical waveguides with multipolar components[43–45] or guiding orbital angular momentum (OAM) modes,[46,47] among others. We focus on the latter, which additionally allows for a simple method to add the impurities experimentally by slightly modifying parameters such as the writing speed in laser-writing setups[48] or the waveguide width in beam lithography setups.[49] The coupling between OAM modes carries a phase that can be used to imprint an artificial gauge field on the system.[46] To build the diamond, we propose to couple modes with different OAM order l in a zig-zag pattern. In particular, modes with $l = 0$ will correspond to the spinal nodes, while modes with $l = \pm 1$ will be split in a synthetic dimension and play the role of top and bottom nodes.[50] In this setup, the relative angle between waveguide pairs will determine the value of the flux, which can be tuned to any desired value.

II. EFFECTIVE IMPURITY SYSTEMS

We briefly summarize the theoretical development outlined in Ref. 24 and in Fig. 1. In particular, we focus on the case of a photonic diamond chain with uniform couplings t and a non-zero reduced magnetic flux across each plaquette, $\phi = 2\pi\frac{\Phi}{\Phi_0}$, where Φ is the magnetic flux and Φ_0 is the magnetic flux quantum. In this scenario, there exists a basis of non-orthogonal CLSs in the FB of the system, each one spanning two plaquettes [see Fig. 1(a)]. Considering the A, B, and C sites consecutively at plaquettes j and $j+1$, the jth normalized CLS has the following form, where "Loc" stands for "Localized,"

$$|\,\mathrm{Loc}, j\rangle = \frac{1}{2}\left(\cdots, 0, 1, -e^{-i\frac{\phi}{2}}, 0, e^{-i\frac{\phi}{2}}, -1, \cdots\right)^T, \tag{1}$$

and is zero elsewhere. As is obvious from expression (1), this CLS will only overlap with the ones at plaquettes $j \pm 1$, with strength $S_{j,j\pm1} = \langle \mathrm{Loc}, j|\mathrm{Loc}, j+1| = \frac{1}{2}\cos\frac{\Phi}{2} = S_{j\pm1,j}$, and thus, the overlap matrix of all localized states will be tridiagonal, with main diagonal elements $S_{j,j} = 1$ from normalization. We now add impurities to the top and bottom sites of a single plaquette at unit cell $q+1$, with $q = N/2$ and N assumed even, of an open diamond chain with $N+1$ unit cells that contains N CLSs in the FB. The corresponding impurity operator has the general form

$$\hat{V} = \varepsilon_B|B_{q+1}\rangle\langle B_{q+1}| + \varepsilon_C|C_{q+1}\rangle\langle C_{q+1}|, \tag{2}$$

where ε_B and ε_C are local impurity potentials, left as free parameters. From here, one may think of building an effective dimer model out of the two CLSs directly affected by the impurity potentials, i.e., $|\mathrm{Loc}, q\rangle$ and $|\mathrm{Loc}, q+1\rangle$. However, the basis of CLSs is not orthogonal, and its orthogonalization leads to modes that are localized but span across several plaquettes. As a consequence, several other modes will also have nonzero weight on the impurity sites, and the effective model will not be restricted to two modes. Alternatively, one might work in the dual basis of localized states found via $|\mathrm{Loc}, i^*\rangle = \sum_j S^{-1}_{i,j}|\mathrm{Loc}, j\rangle$,[24] where $S_{i,j}$ are the elements of the overlap matrix S, with $S^{-1}_{i,j} := [S^{-1}]_{i,j}$. Projecting the impurity operator onto this basis leads to

$$\begin{aligned}\hat{V}_{\mathrm{FB}} &= \sum_{n,m=q}^{q+1} |\,\mathrm{Loc}, n^*\rangle V_{n,m}\langle\,\mathrm{Loc}, m^*| \\ &= v\sum_{n=q}^{q+1}|n^*\rangle\langle n^*| + \left[w|q+1^*\rangle\langle q^*| + \mathrm{H.c.}\right],\end{aligned} \tag{3}$$

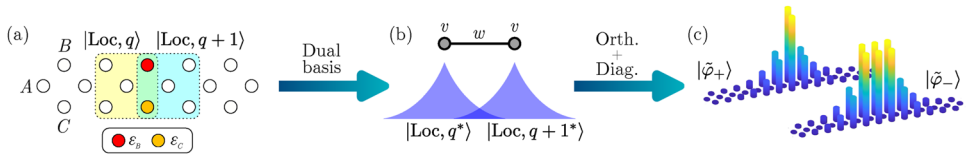

FIG. 1. Summary of the theoretical description of the effective impurity system. (a) The CLSs of the diamond chain located in the two neighboring plaquettes to the one with onsite impurities ε_B and ε_C (yellow and blue shaded regions) have a direct overlap on these sites. However, the CLSs do not constitute an orthogonal basis, so other modes of the FB besides the two CLSs shown in (a) will also have such an overlap when orthogonalizing. To restrict the effective system to two states only, we switch to a dual basis (b) where the impurity operator affects only two localized states that can then be orthogonalized independently to all other modes. Finally, diagonalization of the impurity sub-system leads, when reverted back to the site basis of the chain, to the two exponentially decaying modes in (c), whose amplitude distribution depends on the impurity values and the flux per plaquette.

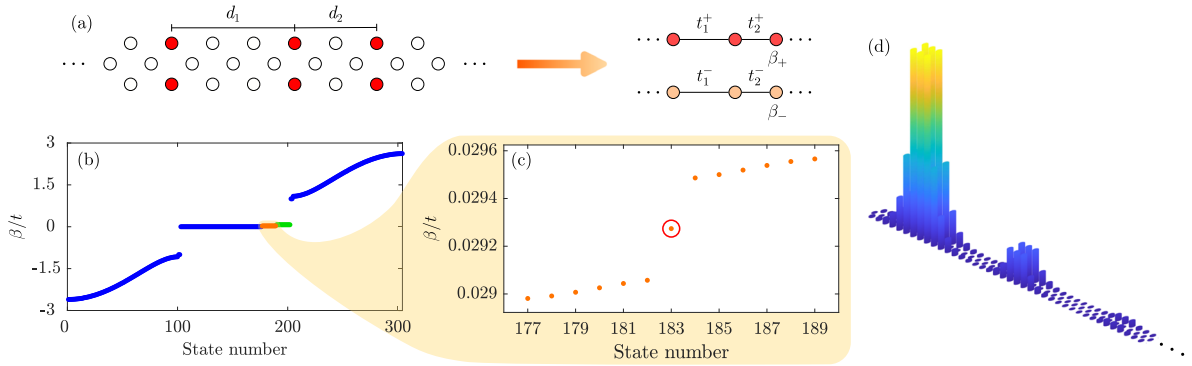

FIG. 2. (a) A diamond chain decorated with a staggered impurity distribution in the top and bottom sites hosts two effective SSH sub-systems. (b) Spectrum of propagation constants for a photonic diamond chain of $N = 101$ unit cells and 13 impurities $\varepsilon_B = \varepsilon_C = \varepsilon = 0.1t$, with $\phi = \pi/2$ and relative distances $d_1 = 8$ and $d_2 = 6$ that yield a coupling ratio of $t_1^-/t_2^- = 0.17$. From the FB, two effective SSH systems centered around different propagation constants (orange and green dots) emerge as a consequence of the coupling of impurity modes. (c) Spectrum of the SSH system with lower propagation constants (orange dots) highlighted in (b). The mode marked with a red circle is its topological edge mode. We show in (d) the absolute value of its amplitudes on each site for a segment of the chain.

where $V_{n,m} = \langle \mathrm{Loc}, n|\hat{V}|\mathrm{Loc}, m\rangle$, and we skip the "Loc" indicator in the second line for brevity. In the dual basis, $v = \frac{\varepsilon_B+\varepsilon_C}{4}$ behaves as a local potential on the dual CLSs at q and $q+1$, and $w = \left(\varepsilon_B e^{-i\frac{\phi}{2}} + \varepsilon_C e^{i\frac{\phi}{2}}\right)/4$ is a coupling term that acts exclusively between them [see Fig. 1(b)]. Therefore, one can now independently orthogonalize the two relevant CLSs and work on a reduced subspace of impurity modes. Following Ref. 24, one can show that for equal impurities $\varepsilon_B = \varepsilon_C = \varepsilon$, the effective impurity matrix in the new orthogonal basis reads

$$\tilde{\mathbf{V}}_{\mathrm{FB}} = \frac{\varepsilon}{2}\left(\sigma_0 + e^{-\theta}\sigma_x\right), \tag{4}$$

where σ_0 is the identity and σ_x is the x Pauli matrix and where $\theta = \cosh^{-1}\left(\sec\frac{\phi}{2}\right)$ contains the flux dependence. Diagonalization of this system leads to the two eigenvectors depicted in Fig. 1(c), with eigenvalues

$$\beta_\pm = \frac{\varepsilon}{2}\left(1 \pm e^{-\theta}\right). \tag{5}$$

As illustrated in the right panel of Fig. 1, these are exponentially decaying modes that are pulled from the FB and that will behave as the main sites of an effective system when decorating the lattice with more impurities. The two modes have different propagation constants within the gap between the FB and the top band, implying that two decoupled copies of the effective system are, in fact, generated, as sketched in Fig. 2(a).

III. RESULTS

A. Effective SSH impurity chains

We consider a diamond chain of $N = 101$ unit cells with nearest-neighbor coupling t and nonzero flux per plaquette ϕ, decorated with a series of 13 impurity pairs in the top and bottom sites, following a staggered pattern as sketched in Fig. 2(a). In particular, we use $d_1 = 8$ and $d_2 = 6$ plaquettes of separation between impurities, with d_1 (d_2) at the left (right) end of the chain. The induced impurity modes couple between themselves forming an effective system. As described in Appendix A, the coupling between the impurity modes depends exponentially on their separation. Therefore, the effective system displays the staggered coupling distribution that is characteristic of the SSH model.[25] We consider the case where the impurities take values $\varepsilon_B = \varepsilon_C = 0.1t$ with a flux of $\phi = \pi/2$. To avoid cutting the exponentially decaying tails of the edge most impurity modes, which would perturb the ends of the effective system, 13 plaquettes before the first impurity pair are left impurity-free at both ends of the chain. As we showcase in Fig. 2(b), two SSH-like subspectra emerge above the FB (orange and green dots). Other choices for the impurity values similarly produce one or two impurity spectra around different propagation constants.[24] In this manuscript, we focus on the spectrum of lower propagation constants (orange dots) in Fig. 2(c), which can be readily recognized to belong to an SSH chain. The highlighted mode in the middle of the gap corresponds to the edge mode of the effective system, whose amplitudes are shown in Fig. 2(d). Interestingly, this edge mode is not localized around the edge of the diamond chain, but rather around the edge of the impurity sub-system.

The features of the effective systems may be controlled by tuning the parameter values of the diamond chain. By choosing an appropriate distribution for the impurities, one may design a wide range of one-dimensional (1D) models. Nonetheless, the flux through each plaquette remains a key property as it affects both the propagation constants and the couplings of the effective system, as can be seen from (4). In particular, the extension of the impurity modes grows for weaker flux as does the coupling between modes localized around adjacent impurity pairs and the gap of the effective system. This fact is proved in Appendix A, where the coupling strength is plotted for varying fluxes and different impurity separations. The changes in the extension of the modes with the flux are further showcased in Ref. 24.

Most notably, the coupling between impurity modes is not limited only to real values and can be pushed into the complex plane by including complex onsite potentials. In particular, one can impose $\varepsilon = |\varepsilon|e^{i\varphi}$, which has two main consequences in the spectrum, as we

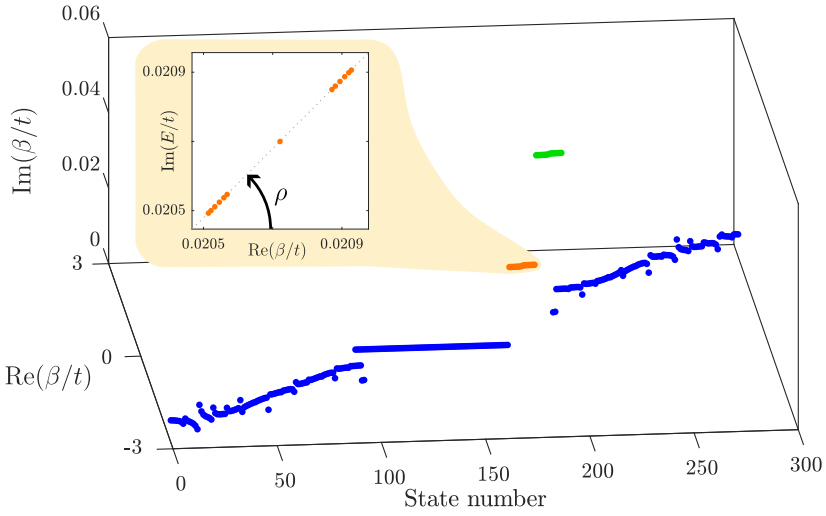

FIG. 3. Complex propagation constant spectrum for the diamond chain with complex onsite impurities $\varepsilon_B = \varepsilon_C = \varepsilon e^{i\rho}$, with $\rho = \pi/4$, and the same lattice parameters as Fig. 2. The spectra of the effective SSH systems rotate along the complex plane by an angle ρ, as can be observed in the inset.

showcase in Fig. 3 for $\rho = \pi/4$. First, all eigenmodes in the conductive bands with finite weight on the impurity sites pick up a small imaginary component in their propagation constants. This effect, however, is nullified when the impurities are balanced, i.e., $\varepsilon_B = -\varepsilon_C$. Second, and more interestingly, the spectra of the effective SSH systems rotate along the complex plane according to the angle ρ, as can be seen in the inset in Fig. 3. By virtue of this rotation, one can readily observe that the effective Hamiltonian of each SSH becomes $\tilde{H}_{\text{eff}} = e^{i\rho} H_{\text{eff}}$ compared to the case of Fig. 2, implying that they are now *non-Hermitian*. This effect could open up the possibility of experimentally exploring non-Hermitian couplings in FB systems by employing lossy impurities, where the coupling strength is determined by the flux per plaquette and the angle of rotation ρ by the included losses.

B. Disorder

Due to the dependence of the extension of the impurity modes on the flux, a disorder on the flux translates into disorder in both the onsite detunings and the couplings of the effective system and, thus, breaks the chiral symmetry of the effective SSH model. We introduce a random flux disorder of strength η in each plaquette, $\phi_j = \phi + \eta_j$, sampled from a uniform distribution $\eta_j \in [-\eta/2, \eta/2]$, as sketched in Fig. 4(a). We explore the consequences of this disorder by checking the variation of the edge mode gap $\Delta = \min(|\beta_q - \beta_{q\pm1}|)$ for the edge mode q of the SSH system in Fig. 2(c) as the perturbation is increased. We plot in Fig. 4(b) the size of this gap and its standard deviation for different values of the central flux ϕ, averaged over 1000 random realizations for each η, in steps of $\Delta\eta = 0.01$ rad.

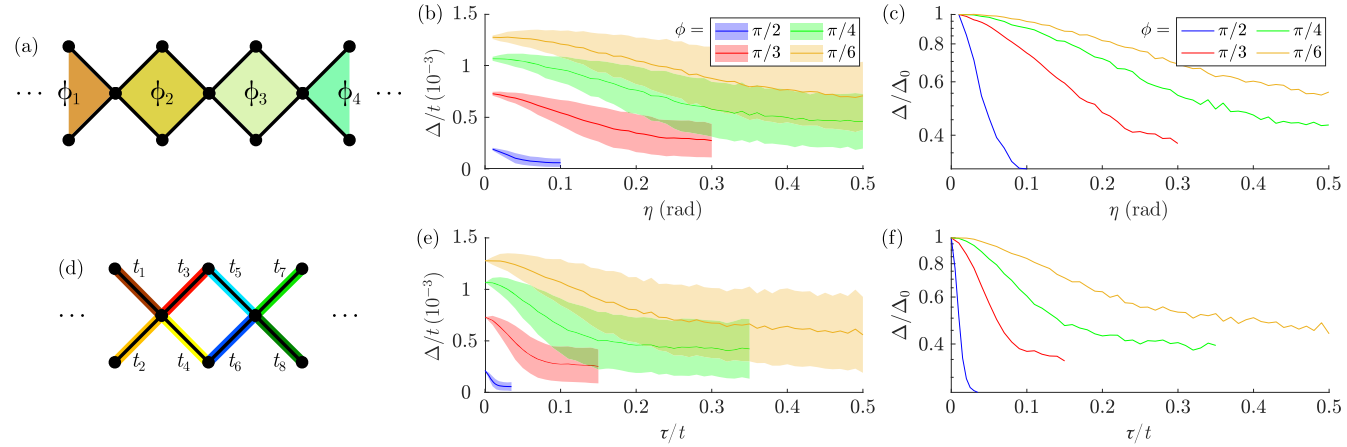

FIG. 4. Effects of disorder on the spectrum of the effective system of Fig. 2(a). (a) Sketch of flux disorder, where each plaquette is threaded by a random flux centered around ϕ. (b) Average gap size Δ of the edge mode of the effective SSH model (solid lines) and standard deviation (shaded region) for increasing flux disorder strengths and different values of ϕ. (c) Disordered gap size Δ relative to the clean system's gap Δ_0 for different values of ϕ. (d) Sketch of uncorrelated coupling disorder, where each link displays a random coupling sampled uniformly around t. (e) Average gap size (solid lines) and standard deviation (shaded regions) for uncorrelated coupling disorder for the same central flux values ϕ as in (b). (f) Gap size relative to the clean system's gap for uncorrelated coupling disorder.

We see that disorder distorts the effective system, reducing the gap, on average, for increasing flux disorder. In general, however, for a weak ϕ, the system displays a larger gap that is also more resilient to disorder compared to fluxes closer to π. This is made evident in Fig. 4(c), where the average gap is compared to the one for the pristine system, Δ_0, for different values of ϕ. The plot shows how weaker fluxes display a slower decay, even for values of disorder of the same order as ϕ itself. This behavior is closely related to the extension of the impurity modes. Although flux disorder breaks chiral symmetry, the impurity modes feel the effects of an averaged disorder over their whole characteristic length,[51] which tends to the effective restoration of chiral symmetry. This average effect becomes stronger for longer extensions, implying an overall weaker effect of the disorder, hence explaining the higher robustness against it as one reduces the flux.[24] The flux-dependent extension of the impurity modes thus becomes a pivotal property of the system.

On the other hand, when disorder in the couplings on the diamond chain is introduced in a correlated manner, as detailed in Appendix B, this translates into off-diagonal disorder in the effective system, against which it is protected. In contrast, completely uncorrelated coupling disorder, as sketched in Fig. 4(d), affects the amplitude distribution of the CLSs themselves as well as their overlap,[24] thus affecting the effective impurity system in a similar manner to flux disorder. We prove this fact by including a random coupling disorder in each link such that $t_j = t + \tau_j$ for $\tau_j \in [-\tau/2, \tau/2]$. In Figs. 4(e) and 4(f), we plot the average gap size and its standard deviation for different values of ϕ and its comparison with the one on the pristine system, respectively. Following the trend depicted in Figs. 4(b) and 4(c) for flux disorder, we observe how uncorrelated coupling disorder heavily affects the spectrum and the gap of the effective system but is partially resisted, on average, for low fluxes even for disorder strengths up to 50% of the value of t. In contrast and as we showcase in Appendix B, the effective system is protected against correlated disorder due to its chiral symmetry. Results for the other non-highlighted sub-system are similar to those depicted here. Nonetheless, when comparing the two systems, the one with lower propagation constants displays higher robustness to disorder owing to the higher extension of its modes that enhances the disorder averaging effect.[24]

IV. IMPLEMENTATION

We consider a zig-zag chain of optical waveguides with a relative distance of d and a staggered relative angle of θ, as depicted in Fig. 5(a). These will guide orbital angular momentum (OAM) modes of the form

$$\Psi^{\pm l}(r, \varphi, z) = \psi^{\pm l}(r) e^{\pm i l(\varphi - \varphi_0)} e^{-i\beta_l z}, \tag{6}$$

where l is the OAM charge, (r, φ, z) are the cylindrical coordinates centered at each waveguide, $\psi^{\pm l}(r)$ is the radial mode profile, φ_0 is an arbitrary phase origin, and β_l is the propagation constant of the mode. According to the modes that are guided in each case, we will consider two types of waveguides. The first set [lower row in Fig. 5(a)] will guide only the fundamental $l = 0$ mode, while the second set [upper row in Fig. 5(a)] will also guide the $l = \pm 1$ modes. By tuning the refractive index contrast of both sets, one can achieve phase matching between the aforementioned $l = 0$ and $l = \pm 1$ modes. In such a scenario, this subset of modes forms an effective diamond chain model by considering the mode circulations as a synthetic dimension. The $l = 0$ modes become the central sites and the $l = \pm 1$ modes become the top and bottom sites of the diamond, respectively, as shown in the right-hand side of Fig. 5(a). Furthermore, it is known that the coupling between OAM modes picks up a phase according to their momentum charge and their circulation, as well

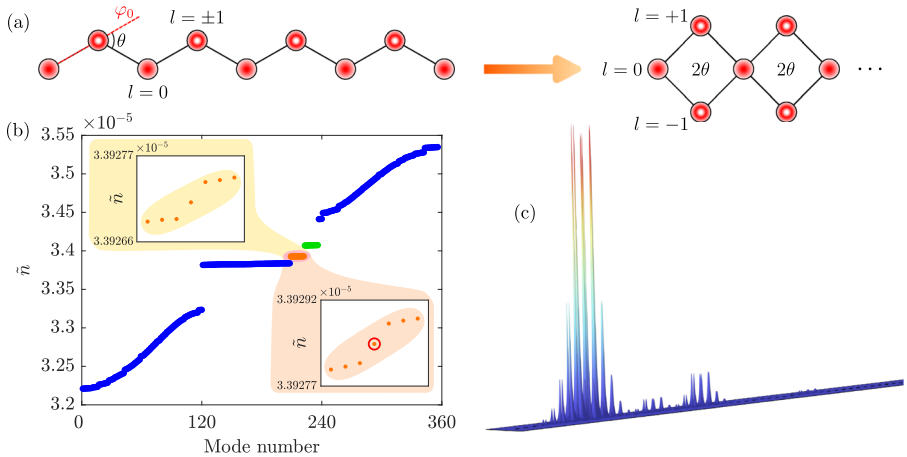

FIG. 5. Implementation of the effective SSH model in a lattice of waveguides hosting OAM modes. (a) Coupled optical waveguides forming a zig-zag chain with alternating $l = 0$ and $l = \pm 1$ OAM charges and a staggered relative angle θ with respect to the reference axis φ_0, which behaves as diamond chain lattice with a flux per plaquette of 2θ. The $l = \pm 1$ modes can be split in a synthetic dimension that forms the top and bottom sites of the diamond. (b) Spectrum of effective mode indices with respect to the cladding index, $\tilde{n} = n_{\text{eff}} - n_0$, for a waveguide lattice of $N = 59$ unit cells, a relative angle of $\theta = \pi/4$ ($\phi = \pi/2$), and 13 impurity pairs in a staggered pattern $d_1 = 8$ and $d_2 = 6$. The insets highlight the lower SSH sub-system (orange dots). Since each waveguide can host two orthogonal mode polarizations, the eigensolver picks up two orthogonal spectra for each SSH system and the spectrum appears doubled. (c) Electric field norms on each waveguide for the edge mode circled in red in (b).

as the coupling angle θ with respect to an arbitrary direction φ_0 [see Fig. 5(a)], i.e., $t_{l_1,l_2} = te^{i(l_1-l_2)\theta}$.[52–54] Considering our geometry and that we are coupling $l_1 = \pm 1$ and $l_2 = 0$ modes, this implies a flux per plaquette of twice the geometric angle 2θ throughout the diamond chain. Therefore, any arbitrary value for the flux can be generated by tuning this angle. The implementation of the system in Fig. 2(a) is completed by perturbing the refractive index of the $l = \pm 1$ waveguides. Since the two OAM components that form the top and bottom sites in the diamond come from the same physical waveguide, we are limited to a symmetric impurity $\varepsilon_B = \varepsilon_C = \varepsilon$ distribution in the effective system.

For our numerical simulations, we consider cylindrical waveguides of radius $R = 12$ μm separated by a relative distance $d = 55$ μm and with a cladding refractive index of $n = 1.48$. The $l = 0$ waveguides display a contrast of $\Delta n_0 = 10^{-4}$, and the matching contrast for $l = \pm 1$ waveguides is computed to be $\Delta n_1 = 2.579 \times 10^{-4}$ for a wavelength of $\lambda = 730$ nm. We impose small impurities on top of some $l = \pm 1$ waveguides by adding an additional contrast of $\Delta n_{\text{imp}} = 6 \times 10^{-7}$ at alternating distances of 8 and 6 unit cells to achieve the staggering and choose a relative angle of $\theta = \pi/4$ equivalent to a flux value of $\phi = \pi/2$. Using these parameter values, we simulate a chain of $N = 59$ unit cells using the commercial finite-element solver COMSOL Multiphysics. We consider fewer unit cells compared with the results in Sec. III due to the limitation of computational memory allocation, but this does not affect the generality of the results. As depicted in Fig. 5(b), we obtain the eigenmodes of the structure, closely matching those obtained in the tight-binding model. The insets of the figure show that we obtain a doubled spectrum, which is due to the orthogonal mode polarizations that can be guided by the waveguide structure. These have similar mode profiles but different projections (E_x, E_y, E_z) and are both picked up by the eigensolver. We showcase in Fig. 5(c) the amplitudes $|E|$ in the waveguide system of the highlighted edge mode in the bottom right inset of Fig. 5(b).

The simulations display a very good agreement with the theoretical results. However, there exist two possible sources of discrepancy with the original model in the form of additional couplings. For the limiting case of $\theta = \pi/2$ and thus a flux of π, the next-nearest neighbor (NNN) distance between waveguides becomes as short as $\sqrt{2}d$. Even then, considering their exponentially decaying nature, the NNN couplings are usually neglected.[46] We show in Appendix C that they are an order of magnitude lower than the main coupling t, but nonetheless they perturb the bands of the system and cause some modes of the flat band to tilt to lower propagation constants. Since our method relies on pulling CLSs from this flat band, we limit ourselves to angles smaller than $\pi/4$ (and thus fluxes smaller than $\pi/2$) where these couplings are already two orders of magnitude lower than t and therefore can be safely ignored. Another effect of interest is the appearance of self-couplings within the $l = \pm 1$ waveguides due to the breaking of the cylindrical symmetry by the presence of other nearby waveguides.[52] In Appendix C, we prove how these self-couplings are around two orders of magnitude lower than t for our parameter values, so they also have a negligible effect on our system.

Finally, we consider the stability of the method to imperfections in the waveguides that deviate from a perfect cylindrical shape. Previous experimental studies[46] have shown that even when deviating from perfect cylindrical waveguides, OAM couplings can still generate an artificial gauge field as observed through the Aharonov–Bohm caging effect. Of course, the shape of the vortices deteriorates due to the ellipticity as the propagation distance increases. As shown in Ref. 47, for elliptical waveguides, $l = \pm 1$ modes are no longer exact eigenmodes of the system and a coupling that we denote as τ_1 appears between them due to the breaking of the cylindrical symmetry in the waveguide. In Appendix D, we detail the finite-element simulations performed for a slight ellipticity in two scenarios: with the major semiaxis aligned (a) with the global x-axis and (b) with the coupling line [see Figs. 12(a) and 12(b)]. As shown in Appendix D, in case (a), τ_1 has a phase, which perturbs the flux through each plaquette and heavily distorts the bands of the system. Conversely, in (b), τ_1 is real, and the system can withstand ellipticities that are an order of magnitude larger without major band deformation. A clear conclusion can be extracted from these results: even if the OAM coupling scheme is sensitive to the cylindrical symmetry of the waveguides, if the ellipticity that is produced during fabrication is known, one can reduce its effects on the effective system by aligning the major axis to the coupling line. Experimentally, the challenge of obtaining perfectly cylindrical waveguides is thus substituted by a problem of waveguide alignment.

V. CONCLUSIONS

We have demonstrated a method to engineer a system with a fine-tuned coupling distribution from the CLSs of a FB lattice, whose parameters are controlled via the flux that threads the plaquettes of the original system. By decorating the FB lattice with onsite impurities, CLSs can be made to couple, giving rise to an effective system in the subspace of exponentially decaying impurity modes. An appropriate choice for the impurity positions leads to a manifestation of non-trivial topology and the appearance of edge modes. To exemplify the method, we imprint an SSH model on top of a diamond chain lattice with nonzero flux per plaquette. By alternating the relative distance between impurities, the characteristic staggered coupling distribution of the SSH model, with its chiral nature, is achieved. We then study the behavior of the effective system when disorder of two kinds is introduced in the system. When correlated coupling disorder is applied and, thus, chiral symmetry is preserved, the effective system is immune to it. On the other hand, when flux disorder or uncorrelated coupling disorder is introduced, chiral symmetry is no longer satisfied. Nonetheless, owing to the large spatial extension of the impurity modes, the disorder is averaged out over their characteristic lengths, which, in turn, implies a lower distortion of the spectrum of the effective system.[51] This effect of enhanced robustness to chiral-breaking disorder is also amplified at lower fluxes, where the extension of the modes is larger.[24]

Additionally, we provide a route for an experimental implementation of the proposed system using optical waveguides guiding light with OAM. The coupling of different OAM modes introduces a phase component in the couplings by controlling the geometric angle between waveguides. This phase serves as an artificial gauge field that provides the necessary flux to the system. Moreover, the different circulations of $l = \pm 1$ OAM modes are used as a synthetic dimension and translated as the top and bottom sites of the diamond chain, while $l = 0$ modes form the central sites. The onsite impurities can be included by manipulating the propagation constant of the

corresponding waveguides. We note that a proposal for implementing the diamond chain was also independently put forward in Ref. 55, but the role or the implementation of impurities that allows us to engineer the effective systems was not considered there. The proposed platform gives complete freedom over the choice of the flux per plaquette, closely replicating the diamond chain for fluxes lower than $\pi/2$ and with minor band distortions for fluxes nearing π. We also perform an analysis of how the effects that deviations from ellipticity in the waveguides have on the spectrum of the system can be reduced, if the ellipticity is known, by aligning the elongation to the coupling line between waveguides.

The method for generating effective models by impurity decorating flat band systems with non-orthogonal bases can be readily generalized to higher-dimensional systems. Furthermore, and as exemplified here, effective non-Hermitian couplings are also easily achievable by including onsite gains and losses at the impurity sites of the underlying lattice, opening a promising FB-based venue for the study of non-Hermitian physics. This adds an alternative to other existing proposals to induce non-Hermitian couplings,[56–58] such as through adiabatic elimination of auxiliary modes with complex refractive indices[59,60] or by introducing gain and loss gradients in two-dimensional (2D) cavities.[61] Aside from optical waveguides, other platforms capable of controlling the phase of the couplings, such as ring resonators, could be well suited for an alternative experimental implementation.

ACKNOWLEDGMENTS

D.V. and V.A. acknowledge financial support from the Spanish State Research Agency AEI (Contract No. PID2020-118153GBI00/AEI/10.13039/501100011033) and Generalitat de Catalunya (Contract No. SGR2021-00138). D.V. acknowledges financial support from Ministerio de Ciencia e Innovación with funding from European Union NextGenerationEU (PRTR-C17.I1). A.M.M. and R.G.D. developed their work within the scope of Portuguese Institute for Nanostructures, Nanomodelling and Nanofabrication (i3N) Project Nos. UIDB/50025/2020, UIDP/50025/2020, and LA/P/0037/2020, financed by national funds through the Fundação para a Ciência e Tecnologia (FCT) and the Ministério da Educação e Ciência (MEC) of Portugal. A.M.M. acknowledges financial support from i3N through Contract No. CDL-CTTRI-46-SGRH/2022 and from FCT through Contract No. CDL-CTTRI-91-SGRH/2024.

AUTHOR DECLARATIONS

Conflict of Interest

The authors have no conflicts to disclose.

Author Contributions

D. Viedma: Conceptualization (equal); Formal analysis (equal); Investigation (equal); Methodology (equal); Software (equal); Writing – original draft (equal); Writing – review & editing (equal). **A. M. Marques**: Conceptualization (equal); Formal analysis (equal); Investigation (equal); Methodology (equal); Writing – review & editing (equal). **R. G. Dias**: Conceptualization (equal); Formal analysis (equal); Funding acquisition (equal); Supervision (equal); Writing – review & editing (equal). **V. Ahufinger**: Conceptualization (equal); Formal analysis (equal); Funding acquisition (equal); Supervision (equal); Writing – review & editing (equal).

DATA AVAILABILITY

The data that support the findings of this study are available from the corresponding author upon reasonable request.

APPENDIX A: COUPLING BETWEEN IMPURITY MODES

To check the exact dependence of the coupling between different impurity modes, we place two sets of equal impurities on different plaquettes in the diamond chain. To extract the coupling, we check the gap between the two induced impurity modes with lower propagation constants as we change the relative distance and define the coupling as

$$\tau = \frac{1}{2}(\beta_+ - \beta_-), \tag{A1}$$

with β_+ (β_-) being the propagation constant of the higher (lower) mode. We plot the obtained coupling dependence with the distance between impurities in Fig. 6(a), where we observe that it displays an exponential dependence on their separation, confirmed also by the inset. We also see that the decaying of the curves is slower for smaller fluxes, in agreement with the larger extension that the impurity modes present.[24] This is further proved in Fig. 6(b), where we now plot the coupling with respect to the flux for different separations. Since the coupling is larger for lower fluxes, the extension

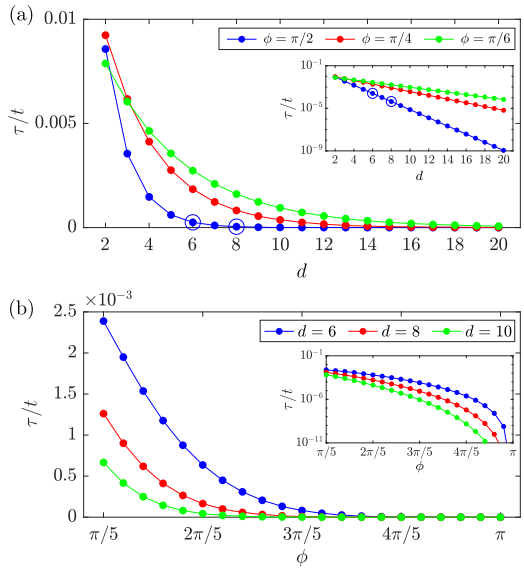

FIG. 6. (a) Coupling strength between two sets of impurities with $\varepsilon_B = \varepsilon_C = 0.1t$ with respect to the number of plaquettes separating them for different flux values. The inset shows the same curves in a logarithmic scale. The coupling values chosen for Fig. 2(b) in the main text, namely, those for $d_1 = 6$ and $d_2 = 8$ for $\phi = \frac{\pi}{2}$, are highlighted with blue circles. (b) Coupling strength for the same impurity values, this time for varying fluxes and fixed impurity distances. The higher extension of the modes for lower fluxes is reflected by the increased coupling strengths.

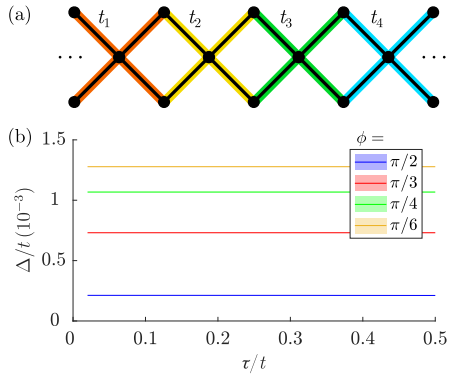

FIG. 7. Effects of correlated coupling disorder on the spectrum of the effective system. (a) Sketch of the considered disorder, introduced in quartets as indicated by the different link colors. (b) Average gap size Δ of the edge mode of the effective SSH model (solid lines) and standard deviation (shaded region) for different flux values. In this scale, the shaded region is too thin to be observed.

of the modes is necessarily larger as well. The curves in Fig. 6 allow us to build a map between couplings and distances, which can also be tuned by controlling the flux on the lattice. Based on it, any coupling distribution can be engineered. The plot for the set of impurity modes with higher propagation constants presents very similar results as those depicted in Fig. 6. This may seem counter-intuitive, considering the fact that the lower modes possess a comparatively larger extension. The amplitudes of the impurity modes of higher and lower propagation constants for different fluxes can be found in Ref. 24. When numerically computing the coupling, the different behavior of the central peak at the plaquette hosting the impurities as well as the exponential amplitude tails in both cases seems to lead to approximately equal results.

APPENDIX B: CORRELATED COUPLING DISORDER

As described in the main text, coupling disorder only behaves as chiral for the effective system when introduced in a correlated manner. As CLSs occupy two plaquettes for fluxes between 0 and π, any coupling disorder within the span of each CLS will affect their amplitudes and propagation constants, hence breaking the chiral symmetry of the effective system. For the disorder to be chiral, it has to be introduced in hopping quartets,[30] as highlighted in Fig. 7(a), so that it may affect the coupling between impurity modes without distorting the CLSs themselves. We plot in Fig. 7(b) the effects of this disorder on the gap size of the effective system. Comparing with Fig. 4 in the main text, we observe that the edge mode gap is immune to correlated disorder even for $\phi = \pi/2$.

APPENDIX C: COUPLING BETWEEN OAM MODES

As described in Ref. 52, symmetry considerations reduce the number of independent components in the analysis of the coupling between OAM modes. In addition to the nearest-neighbor couplings discussed in the main text, one may also consider the effect of longer-range couplings between the closest waveguides of the same

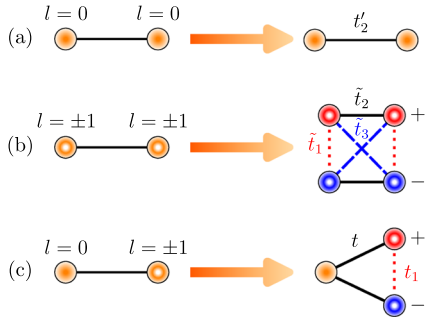

FIG. 8. Coupling scheme between waveguides with different OAM modal content. The left-hand side corresponds to the physical waveguides, whereas in the right-hand side, different OAM circulations are represented separately.

type. Hence, for our purposes, it is enough to consider the following three scenarios: (a) $l = 0 \leftrightarrow l = 0$, (b) $l = \pm 1 \leftrightarrow l = \pm 1$, and (c) $l = 0 \leftrightarrow l = \pm 1$, as sketched in Fig. 8. All cases can be described via at most three independent couplings: between different OAM components in the same waveguide, t_1, between the same OAM component in different waveguides, t_2, and between different components in different waveguides, t_3. These depend on the overlap integral between the relevant modes, and t_1 and t_3 are also subject to picking up a phase depending on their OAM charge and the relative angle with respect to an arbitrary origin φ_0.[52] The first coupling, t_1, appears due to the breaking of the cylindrical symmetry of the waveguide mode due to the presence of the second waveguide. We specify all possible next-nearest-neighbor (NNN) components that appear in our system in Fig. 9, with their corresponding phases. Note that the geometrical angle between $l = \pm 1$ waveguides is half as large as the one between $l = 0$ and $l = \pm 1$.

We now describe how to compute these couplings from the eigenvalues of the tight-binding model generated by the couplings in Figs. 8(a)–8(c). For case (a), the Hamiltonian is given by

$$H_{l=0} = \begin{pmatrix} \beta_0 & t_2' \\ t_2' & \beta_0 \end{pmatrix}, \tag{C1}$$

whose eigenvalues are $\lambda_- = \beta_0 - t_2'$ and $\lambda_+ = \beta_0 + t_2'$, and thus,

$$t_2' = \frac{1}{2}(\lambda_+ - \lambda_-). \tag{C2}$$

The Hamiltonian for case (b) is written as

$$H_{l=1} = \begin{pmatrix} \beta_1 & \tilde{t}_1 & \tilde{t}_2 & \tilde{t}_3 \\ \tilde{t}_1 & \beta_1 & \tilde{t}_3 & \tilde{t}_2 \\ \tilde{t}_2 & \tilde{t}_3 & \beta_1 & \tilde{t}_1 \\ \tilde{t}_3 & \tilde{t}_2 & \tilde{t}_1 & \beta_1 \end{pmatrix}, \tag{C3}$$

whose eigenvalues are

$$\begin{aligned} \lambda_1 &= \beta_1 + \tilde{t}_1 - \tilde{t}_2 - \tilde{t}_3, \\ \lambda_2 &= \beta_1 - \tilde{t}_1 + \tilde{t}_2 - \tilde{t}_3, \\ \lambda_3 &= \beta_1 - \tilde{t}_1 - \tilde{t}_2 + \tilde{t}_3, \\ \lambda_4 &= \beta_1 + \tilde{t}_1 + \tilde{t}_2 + \tilde{t}_3, \end{aligned} \tag{C4}$$

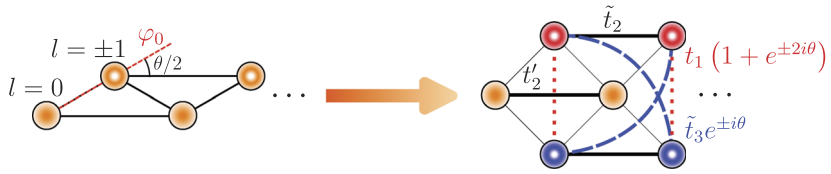

FIG. 9. Full coupling scheme in the effective diamond chain featured in the main text, including the phases induced by the geometrical angle. The NN couplings are also sketched for clarity. Cross-circulation couplings in the $l = \pm 1$ waveguides due to the nearest $l = \pm 1$ waveguides, $\tilde{t}_1$, are much smaller than t_1 and are thus not included.

and thus, the couplings can be determined as

$$\begin{aligned} \tilde{t}_1 &= \lambda_1 - \lambda_2 - \lambda_3 + \lambda_4, \\ \tilde{t}_2 &= -\lambda_1 + \lambda_2 - \lambda_3 + \lambda_4, \\ \tilde{t}_3 &= -\lambda_1 - \lambda_2 + \lambda_3 + \lambda_4. \end{aligned} \tag{C5}$$

Finally, for case (c), we have

$$H_{l=0,1} = \begin{pmatrix} \beta_2 & t & t \\ t & \beta_2 & t_1 \\ t & t_1 & \beta_2 \end{pmatrix}, \tag{C6}$$

for which the eigenvalues are

$$\begin{aligned} \lambda_1 &= \beta_2 - t_1, \\ \lambda_2 &= \beta_2 + \frac{1}{2}\left(t_1 - \sqrt{t_1^2 + 8t^2}\right), \\ \lambda_3 &= \beta_2 + \frac{1}{2}\left(t_1 + \sqrt{t_1^2 + 8t^2}\right), \end{aligned} \tag{C7}$$

and the couplings read

$$\begin{aligned} t_1 &= \frac{1}{3}(-2\lambda_1 + \lambda_2 + \lambda_3), \\ t &= \sqrt{\frac{(\lambda_3 - \lambda_2)^2 - (-2\lambda_1 + \lambda_2 + \lambda_3)^2/9}{8}}. \end{aligned} \tag{C8}$$

We perform finite-element simulations of the waveguides described in the main text at different distances and compute the coupling strengths using expressions (C2), (C5), and (C8), as displayed in Fig. 10. Using the computed values, we can estimate the importance of the additional couplings not taken into account in the main text and thus the deviation of the implementation from a pure diamond chain. For a relative distance of $d = 55$ μm, the nearest-neighbor (NN) coupling has a value of $t = 5.08$ m^{-1} and the cross-circulation coupling at the same distance is $t_1 = -0.12$ m^{-1} $= -0.024t$. Depending on the chosen angle θ, the NNN distance d' will vary. We summarize the NNN couplings for $\theta = \pi/2$ ($d' = 77.8$ μm) and $\theta = \pi/4$ ($d' = 101.64$ μm) in Table I. We do not include the cross-circulation coupling $\tilde{t}_1$ as it is at least an order of magnitude lower than the others at all distances.

TABLE I. NNN coupling strength values for different flux values, relative to the value for the NN coupling at $d = 55$ μm.

	$\phi = \pi$ (%)	$\phi = \pi/2$ (%)
$t_2'(l = 0 \leftrightarrow l = 0)$	12.82	2.58
$\tilde{t}_2(l = \pm 1 \leftrightarrow l = \pm 1)$	9.04	1.82
$\tilde{t}_3(l = \pm 1 \leftrightarrow l = \mp 1)$	12	2.58

With the coupling strengths in Table I, we simulate the tight-binding model of a diamond chain model with NNN and cross-circulation couplings (see Fig. 9) and compare the obtained spectrum with a system with only NN couplings in Fig. 11. For fluxes close to π, where the geometrical angle is large and thus the NNN distances are relatively small, the deformation of the bands is evident. In Fig. 11(a), one can observe that the top and bottom bands are not flat, but rather dispersive, as is a sizable portion of the central band. Conversely, for $\phi = \pi/2$ and lower, the deviations caused by these couplings become much smaller and increasingly negligible. Therefore, we limit the study to $0 < \theta \leq \frac{\pi}{4}$ (corresponding to $0 < \phi \leq \frac{\pi}{2}$), where only the NN couplings mentioned in the main text play a significant role.

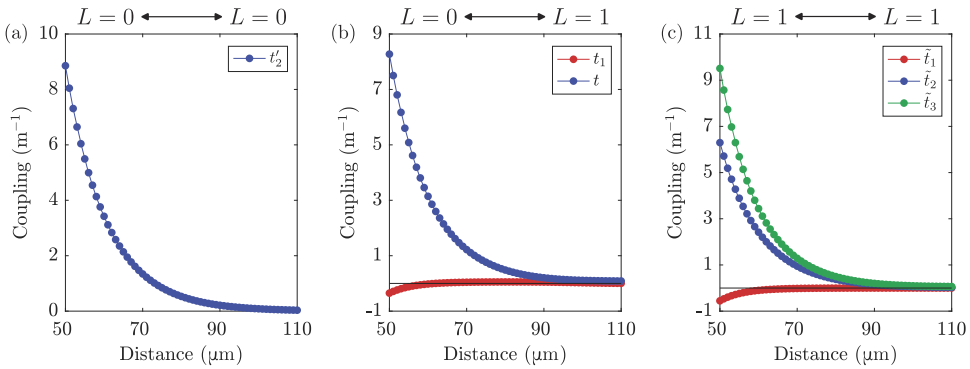

FIG. 10. Coupling strengths between waveguides with different OAM modal content at increasing relative distances for the waveguide parameter values included in the main text. The t_1 coupling is at least an order of magnitude lower than the rest at all distances, both in (b) and (c).

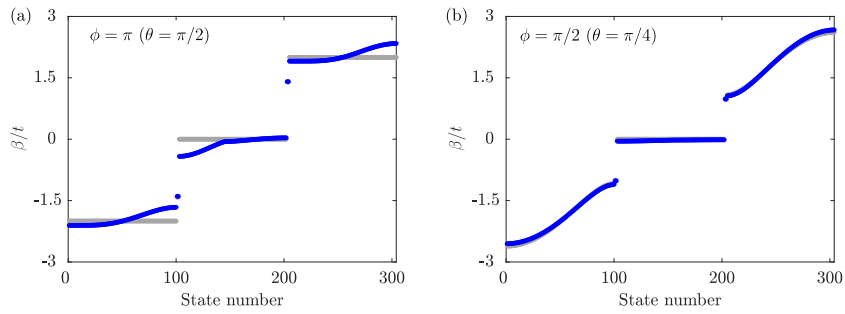

FIG. 11. Spectrum of propagation constants of the diamond chain for (a) $\phi = \pi$ ($\theta = \pi/2$) and (b) $\phi = \pi/2$ ($\theta = \pi/4$) using the coupling strengths obtained from the waveguide simulations in Fig. 10 at $d = 55\ \mu$m and for $N = 101$ plaquettes. The spectrum in blue corresponds to a system with both a cross-circulation coupling and the NNN couplings included in Table I, whereas the gray spectrum corresponds to a system with only NN couplings.

APPENDIX D: ELLIPTICAL WAVEGUIDES

We consider the same zig-zag chain of optical waveguides as in Sec. IV, with each waveguide presenting a slight ellipticity that breaks the cylindrical symmetry. The waveguides are modeled as equal ellipses with semiaxes a_x and $a_y = C\,a_x$, where the degree of ellipticity is introduced through the parameter C, corresponding to an eccentricity of $\sqrt{1 - C^2}$. We then consider two scenarios for the ellipticity, (a) with a_x being aligned either along the global x-axis or (b) along the waveguide coupling line. These are sketched in Figs. 12(a) and 12(b), respectively. Both cases yield the coupling distribution shown in Fig. 12(c), wherein a new coupling τ_1 among $l = \pm 1$ OAM components in each waveguide appears due to the ellipticity.[47] The main difference lies in the phase of the coupling, which depends on the angle α between a_x and the coupling line, and is thus equal to 2ϕ in (a) and to zero in (b). Note that by increasing the ellipticity, we are effectively modifying the propagation constants of $l = 0$ and $l = \pm 1$ in an unequal way. To avoid including extra detunings to the analysis, the matching of refractive indices has to be performed for each considered ellipticity.

We perform finite-element simulations for both cases and a slight ellipticity of $C = 0.998$ and show the photonic bands of both systems in Fig. 12(d), where the gray dots correspond to case (a) and the blue dots correspond to case (b). From these results, it is clear

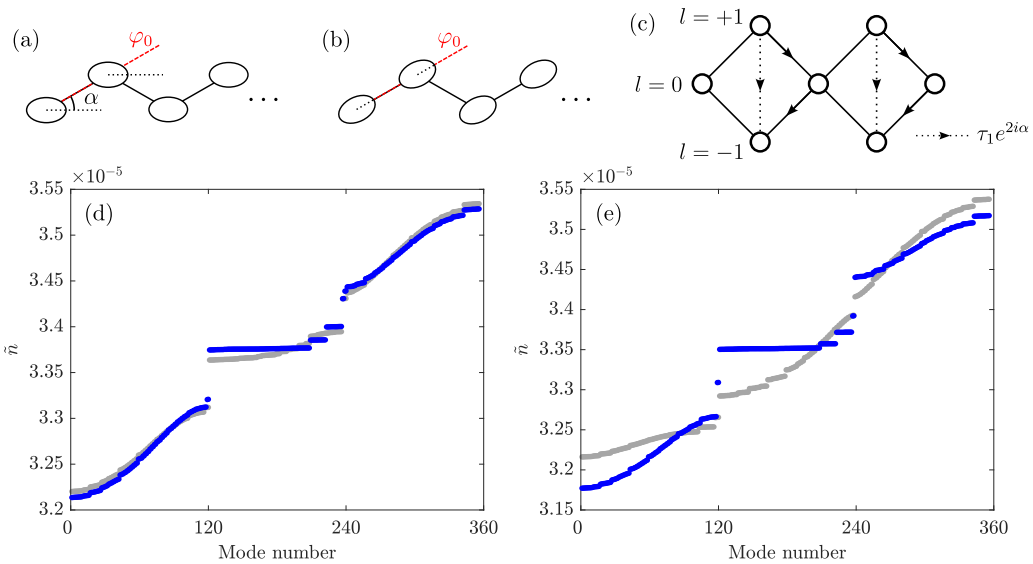

FIG. 12. (a) and (b) Sketch of a zig-zag chain of elliptical waveguides, with the major semiaxis a_x aligned with (a) the global x-axis and (b) the coupling line. The considered ellipticity is exaggerated for visualization purposes. (c) Coupling scheme corresponding to the waveguide chain, where the phase of the vertical coupling τ_1 depends on the orientation of the ellipses. (d) and (e) Spectrum of effective mode indices with respect to the cladding index, $\tilde{n} = n_{\text{eff}} - n_0$, for a chain of $N = 59$ unit cells with the same impurities and parameter values as Fig. 5. The waveguides are now elliptical with a parameter (d) $C = 0.998$ and (e) $C = 0.99$. Gray dots correspond to the case in (a), and blue dots correspond to the case in (b).

that even low ellipticities can have an effect on the effective system, with the primary distorting effect being the phase in the τ_1 coupling. In case (a), the flat band becomes tilted and merges with the lower effective system. For case (b), where this phase is not present, little to no deformation is observed in the bands. If we increase the ellipticity an additional order of magnitude, to $C = 0.99$, the same tendency appears. In Fig. 12(e), the gray dots of case (a) present major band deformations to the point where the effective systems are no longer recognizable. In remarkable contrast, the blue dots of case (b) show only minor deformations of the lower effective system. The higher one, with larger detuning, resists these effects better. In all cases, the effects of the ellipticity on the effective systems could be reduced by employing larger impurities.

REFERENCES

[1] D. Leykam and S. Flach, "Perspective: Photonic flatbands," APL Photonics **3**, 070901 (2018).
[2] R. A. Vicencio Poblete, "Photonic flat band dynamics," Adv. Phys.:X **6**, 1878057 (2021).
[3] D. Leykam, A. Andreanov, and S. Flach, "Artificial flat band systems: From lattice models to experiments," Adv. Phys.:X **3**, 1473052 (2018).
[4] J. Yang, P. Zhang, M. Yoshihara, Y. Hu, and Z. Chen, "Image transmission using stable solitons of arbitrary shapes in photonic lattices," Opt. Lett. **36**, 772–774 (2011).
[5] R. A. Vicencio and C. Mejía-Cortés, "Diffraction-free image transmission in kagome photonic lattices," J. Opt. **16**, 015706 (2013).
[6] T. Baba, "Slow light in photonic crystals," Nat. Photonics **2**, 465–473 (2008).
[7] J. Li, T. P. White, L. O'Faolain, A. Gomez-Iglesias, and T. F. Krauss, "Systematic design of flat band slow light in photonic crystal waveguides," Opt. Express **16**, 6227–6232 (2008).
[8] S. A. Schulz, J. Upham, L. O'Faolain, and R. W. Boyd, "Photonic crystal slow light waveguides in a kagome lattice," Opt. Lett. **42**, 3243–3246 (2017).
[9] Y. Yang, C. Roques-Carmes, S. E. Kooi, H. Tang, J. Beroz, E. Mazur, I. Kaminer, J. D. Joannopoulos, and M. Soljačić, "Photonic flatband resonances for free-electron radiation," Nature **613**, 42–47 (2023).
[10] S. Mukherjee, A. Spracklen, D. Choudhury, N. Goldman, P. Öhberg, E. Andersson, and R. R. Thomson, "Observation of a localized flat-band state in a photonic Lieb lattice," Phys. Rev. Lett. **114**, 245504 (2015).
[11] R. A. Vicencio, C. Cantillano, L. Morales-Inostroza, B. Real, C. Mejía-Cortés, S. Weimann, A. Szameit, and M. I. Molina, "Observation of localized states in Lieb photonic lattices," Phys. Rev. Lett. **114**, 245503 (2015).
[12] H. S. Nguyen, F. Dubois, T. Deschamps, S. Cueff, A. Pardon, J.-L. Leclercq, C. Seassal, X. Letartre, and P. Viktorovitch, "Symmetry breaking in photonic crystals: On-demand dispersion from flatband to Dirac cones," Phys. Rev. Lett. **120**, 066102 (2018).
[13] N. Myoung, H. C. Park, A. Ramachandran, E. Lidorikis, and J.-W. Ryu, "Flatband localization and self-collimation of light in photonic crystals," Sci. Rep. **9**, 2862 (2019).
[14] T. Jacqmin, I. Carusotto, I. Sagnes, M. Abbarchi, D. D. Solnyshkov, G. Malpuech, E. Galopin, A. Lemaître, J. Bloch, and A. Amo, "Direct observation of Dirac cones and a flatband in a honeycomb lattice for polaritons," Phys. Rev. Lett. **112**, 116402 (2014).
[15] S. Xia, Y. Hu, D. Song, Y. Zong, L. Tang, and Z. Chen, "Demonstration of flat-band image transmission in optically induced Lieb photonic lattices," Opt. Lett. **41**, 1435 (2016).
[16] Y. Zong, S. Xia, L. Tang, D. Song, Y. Hu, Y. Pei, J. Su, Y. Li, and Z. Chen, "Observation of localized flat-band states in kagome photonic lattices," Opt. Express **24**, 8877 (2016).
[17] C. C. Abilio, P. Butaud, T. Fournier, B. Pannetier, J. Vidal, S. Tedesco, and B. Dalzotto, "Magnetic field induced localization in a two-dimensional superconducting wire network," Phys. Rev. Lett. **83**, 5102–5105 (1999).
[18] S. Taie, H. Ozawa, T. Ichinose, T. Nishio, S. Nakajima, and Y. Takahashi, "Coherent driving and freezing of bosonic matter wave in an optical Lieb lattice," Sci. Adv. **1**, e1500854 (2015).
[19] R. Drost, T. Ojanen, A. Harju, and P. Liljeroth, "Topological states in engineered atomic lattices," Nat. Phys. **13**, 668–671 (2017).
[20] M. R. Slot, T. S. Gardenier, P. H. Jacobse, G. C. Van Miert, S. N. Kempkes, S. J. Zevenhuizen, C. M. Smith, D. Vanmaekelbergh, and I. Swart, "Experimental realization and characterization of an electronic Lieb lattice," Nat. Phys. **13**, 672–676 (2017).
[21] J. Yang, Y. Li, Y. Yang, X. Xie, Z. Zhang, J. Yuan, H. Cai, D.-W. Wang, and F. Gao, "Realization of all-band-flat photonic lattices," Nat. Commun. **15**, 1484 (2024).
[22] C. Danieli, A. Andreanov, D. Leykam, and S. Flach, "Flat band fine-tuning and its photonic applications," Nanophotonics **13**, 3925 (2024); arXiv:2403.17578 [physics.optics].
[23] W. Maimaiti, A. Andreanov, H. C. Park, O. Gendelman, and S. Flach, "Compact localized states and flat-band generators in one dimension," Phys. Rev. B **95**, 115135 (2017).
[24] A. M. Marques, D. Viedma, V. Ahufinger, and R. G. Dias, "Impurity flat band states in the diamond chain," Commun. Phys. **7**, 387 (2024).
[25] W. P. Su, J. R. Schrieffer, and A. J. Heeger, "Solitons in polyacetylene," Phys. Rev. Lett. **42**, 1698–1701 (1979).
[26] M. Hafezi, E. A. Demler, M. D. Lukin, and J. M. Taylor, "Robust optical delay lines with topological protection," Nat. Phys. **7**, 907–912 (2011).
[27] M. Hafezi, S. Mittal, J. Fan, A. Migdall, and J. M. Taylor, "Imaging topological edge states in silicon photonics," Nat. Photonics **7**, 1001–1005 (2013).
[28] S. Mittal, J. Fan, S. Faez, A. Migdall, J. Taylor, and M. Hafezi, "Topologically robust transport of photons in a synthetic gauge field," Phys. Rev. Lett. **113**, 087403 (2014).
[29] S. Mittal, S. Ganeshan, J. Fan, A. Vaezi, and M. Hafezi, "Measurement of topological invariants in a 2D photonic system," Nat. Photonics **10**, 180–183 (2016).
[30] D. Viedma, A. M. Marques, R. G. Dias, and V. Ahufinger, "Topological n-root Su–Schrieffer–Heeger model in a non-Hermitian photonic ring system," Nanophotonics **13**, 51–61 (2024).
[31] C. J. Flower, M. Jalali Mehrabad, L. Xu, G. Moille, D. G. Suarez-Forero, O. Örsel, G. Bahl, Y. Chembo, K. Srinivasan, S. Mittal, and M. Hafezi, "Observation of topological frequency combs," Science **384**, 1356–1361 (2024).
[32] K. Fang, Z. Yu, and S. Fan, "Realizing effective magnetic field for photons by controlling the phase of dynamic modulation," Nat. Photonics **6**, 782–787 (2012).
[33] S. Longhi, "Effective magnetic fields for photons in waveguide and coupled resonator lattices," Opt. Lett. **38**, 3570 (2013).
[34] M. C. Rechtsman, J. M. Zeuner, Y. Plotnik, Y. Lumer, D. Podolsky, F. Dreisow, S. Nolte, M. Segev, and A. Szameit, "Photonic Floquet topological insulators," Nature **496**, 196–200 (2013).
[35] M. C. Rechtsman, J. M. Zeuner, A. Tünnermann, S. Nolte, M. Segev, and A. Szameit, "Strain-induced pseudomagnetic field and photonic Landau levels in dielectric structures," Nat. Photonics **7**, 153–158 (2013).
[36] Y. Plotnik, M. A. Bandres, S. Stützer, Y. Lumer, M. C. Rechtsman, A. Szameit, and M. Segev, "Analogue of Rashba pseudo-spin-orbit coupling in photonic lattices by gauge field engineering," Phys. Rev. B **94**, 020301 (2016).
[37] Y. Lumer, M. A. Bandres, M. Heinrich, L. J. Maczewsky, H. Herzig-Sheinfux, A. Szameit, and M. Segev, "Light guiding by artificial gauge fields," Nat. Photonics **13**, 339–345 (2019).
[38] M. Parto, H. Lopez-Aviles, J. E. Antonio-Lopez, M. Khajavikhan, R. Amezcua-Correa, and D. N. Christodoulides, "Observation of twist-induced geometric phases and inhibition of optical tunneling via Aharonov-Bohm effects," Sci. Adv. **5**, eaau8135 (2019).
[39] P. S. J. Russell and Y. Chen, "Localization of light in multi-helical arrays of discrete coupled waveguides," Laser Photonics Rev. **17**, 2200570 (2023).
[40] A. Regensburger, C. Bersch, B. Hinrichs, G. Onishchukov, A. Schreiber, C. Silberhorn, and U. Peschel, "Photon propagation in a discrete fiber network: An interplay of coherence and losses," Phys. Rev. Lett. **107**, 233902 (2011).
[41] A. Regensburger, C. Bersch, M.-A. Miri, G. Onishchukov, D. N. Christodoulides, and U. Peschel, "Parity-time synthetic photonic lattices," Nature **488**, 167–171 (2012).

[42]M. Wimmer, H. M. Price, I. Carusotto, and U. Peschel, "Experimental measurement of the berry curvature from anomalous transport," Nat. Phys. **13**, 545–550 (2017).
[43]G. Cáceres-Aravena, D. Guzmán-Silva, I. Salinas, and R. A. Vicencio, "Controlled transport based on multiorbital Aharonov-Bohm photonic caging," Phys. Rev. Lett. **128**, 256602 (2022).
[44]J. Schulz, J. Noh, W. A. Benalcazar, G. Bahl, and G. von Freymann, "Photonic quadrupole topological insulator using orbital-induced synthetic flux," Nat. Commun. **13**, 6597 (2022).
[45]C. Jiang, Y. Song, X. Li, P. Lu, and S. Ke, "Photonic möbius topological insulator from projective symmetry in multiorbital waveguides," Opt. Lett. **48**, 2337 (2023).
[46]C. Jörg, G. Queraltó, M. Kremer, G. Pelegrí, J. Schulz, A. Szameit, G. von Freymann, J. Mompart, and V. Ahufinger, "Artificial gauge field switching using orbital angular momentum modes in optical waveguides," Light: Sci. Appl. **9**, 150 (2020).
[47]C. Jiang, Y. Wu, M. Qin, and S. Ke, "Topological bound modes with orbital angular momentum in optical waveguide arrays," J. Lightwave Technol. **41**, 2205–2211 (2023).
[48]A. Szameit and S. Nolte, "Discrete optics in femtosecond-laser-written photonic structures," J. Phys. B: At., Mol. Opt. Phys. **43**, 163001 (2010).
[49]Y. Chen, "Nanofabrication by electron beam lithography and its applications: A review," Microelectron. Eng. **135**, 57–72 (2015).
[50]E. Nicolau, A. M. Marques, R. G. Dias, J. Mompart, and V. Ahufinger, "Many-body Aharonov-Bohm caging in a lattice of rings," Phys. Rev. A **107**, 023305 (2023).
[51]F. Munoz, F. Pinilla, J. Mella, and M. I. Molina, "Topological properties of a bipartite lattice of domain wall states," Sci. Rep. **8**, 17330 (2018).
[52]J. Polo, J. Mompart, and V. Ahufinger, "Geometrically induced complex tunnelings for ultracold atoms carrying orbital angular momentum," Phys. Rev. A **93**, 033613 (2016).
[53]G. Pelegrí, A. M. Marques, R. G. Dias, A. J. Daley, V. Ahufinger, and J. Mompart, "Topological edge states with ultracold atoms carrying orbital angular momentum in a diamond chain," Phys. Rev. A **99**, 023612 (2019).
[54]G. Pelegrí, A. M. Marques, R. G. Dias, A. J. Daley, J. Mompart, and V. Ahufinger, "Topological edge states and Aharanov-Bohm caging with ultracold atoms carrying orbital angular momentum," Phys. Rev. A **99**, 023613 (2019).
[55]Y. Wang, C. Jiang, M. Zhao, D. Zhao, and S. Ke, "Compact topological edge modes through hybrid coupling of orbital angular momentum modes," Phys. Rev. A **109**, 063516 (2024).
[56]X. Zhou, S. K. Gupta, Z. Huang, Z. Yan, P. Zhan, Z. Chen, M. Lu, and Z. Wang, "Optical lattices with higher-order exceptional points by non-Hermitian coupling," Appl. Phys. Lett. **113**, 101108 (2018).
[57]X. Zhu, H. Wang, S. K. Gupta, H. Zhang, B. Xie, M. Lu, and Y. Chen, "Photonic non-Hermitian skin effect and non-Bloch bulk-boundary correspondence," Phys. Rev. Res. **2**, 013280 (2020).
[58]X. Zhang, T. Zhang, M.-H. Lu, and Y.-F. Chen, "A review on non-Hermitian skin effect," Adv. Phys.:X **7**, 2109431 (2022).
[59]S. Longhi, D. Gatti, and G. D. Valle, "Robust light transport in non-Hermitian photonic lattices," Sci. Rep. **5**, 13376 (2015).
[60]X.-L. Zhang, T. Jiang, and C. T. Chan, "Dynamically encircling an exceptional point in anti-parity-time symmetric systems: Asymmetric mode switching for symmetry-broken modes," Light: Sci. Appl. **8**, 88 (2019).
[61]L. Ge and A. D. Stone, "Parity-time symmetry breaking beyond one dimension: The role of degeneracy," Phys. Rev. X **4**, 031011 (2014).